Journal of Biomedical Optics

BiomedicalOptics.SPIEDigitalLibrary.org

Determining the light scattering and absorption parameters from forward-directed flux measurements in cardiac tissue

Anthony J. Costantino
Christopher J. Hyatt
Michaela C. Kollisch-Singule
Jacques Beaumont
Bradley J. Roth
Arkady M. Pertsov

SPIE.

Anthony J. Costantino, Christopher J. Hyatt, Michaela C. Kollisch-Singule, Jacques Beaumont, Bradley J. Roth, Arkady M. Pertsov, "Determining the light scattering and absorption parameters from forward-directed flux measurements in cardiac tissue," *J. Biomed. Opt.* **22**(7), 076009 (2017), doi: 10.1117/1.JBO.22.7.076009.

Determining the light scattering and absorption parameters from forward-directed flux measurements in cardiac tissue

Anthony J. Costantino,[a] Christopher J. Hyatt,[b] Michaela C. Kollisch-Singule,[c] Jacques Beaumont,[d] Bradley J. Roth,[e] and Arkady M. Pertsov[d,*]
[a]Binghamton University, Department of Electrical and Computer Engineering, Binghamton, New York, United States
[b]Springfield College, Department of Mathematics, Physics and Computer Science, Springfield, Massachusetts, United States
[c]Upstate Medical University, Department of General Surgery, Syracuse, New York, United States
[d]Upstate Medical University, Department of Pharmacology, Syracuse, New York, United States
[e]Oakland University, Department of Physics, Rochester, Michigan, United States

Abstract. We describe a method to accurately measure the light scattering model parameters from forward-directed flux (FDF) measurements carried out with a fiber-optic probe (optrode). Improved determination of light scattering parameters will, in turn, permit better modeling and interpretation of optical mapping in the heart using voltage-sensitive dyes. Using our optrode-based system, we carried out high spatial resolution measurements of FDF in intact and homogenized cardiac tissue, as well as in intralipid-based tissue phantoms. The samples were illuminated with a broad collimated beam at 660 and 532 nm. Measurements were performed with a plunge fiber-optic probe (NA = 0.22) at a spatial resolution of up to 10 μm. In the vicinity of the illuminated surface, the FDF consistently manifested a fast decaying exponent with a space constant comparable with the decay rate of ballistic photons. Using a Monte Carlo model, we obtained a simple empirical formula linking the rate of the fast exponent to the scattering coefficient, the anisotropy parameter g, and the numerical aperture of the probe. The estimates of scattering coefficient based on this formula were validated in tissue phantoms. Potential applications of optical fiber-based FDF measurements for the evaluation of optical parameters in turbid media are discussed. [DOI: 10.1117/1.JBO.22.7.076009]

Keywords: transmission; absorption; scattering; heart; fiber-optic applications; optical mapping.

Paper 170077R received Feb. 6, 2017; accepted for publication Jun. 15, 2017; published online Jul. 14, 2017.

1 Introduction

Current interest in understanding light transport in cardiac tissue has been motivated in part by continued improvements in optical mapping methods over the past two decades. In optical mapping, voltage-sensitive and Ca_i^{2+}-sensitive fluorescent probes are used in conjunction with high-speed imaging devices to map electrical impulse propagation and Ca_i^{2+}-transients in the heart.[1–9] Optical mapping techniques can also be applied to skeletal muscle,[10] smooth muscle,[11,12] and also to monitor neuronal activity in the brain.[13,14]

Optical recordings are usually taken in epifluorescence mode, in which the tissue surface is illuminated with a broad-field source located outside the tissue while the emitted fluorescence is also simultaneously measured outside of the same tissue surface.[15] Significant fluorescent signal contributions from subsurface heart tissue layers, however, are typically present in such experiments.[16,17] Contributions to measured fluorescence arising from subsurface heart tissue layers are particularly significant for recently developed near-infrared voltage-sensitive dyes such as Di-4-ANBDQBS, which have excitation maxima at red wavelengths (~660 nm) and emission maxima at near-infrared wavelengths (~700 to 800 nm).[7,18–20] Subsurface contributions can also be significant for voltage-sensitive dyes excited with green wavelengths (~520 nm), and with emission at red wavelengths (~640 nm), such as Di-4-ANEPPS.[21–24]

The objective of our study was to improve the quantitative interpretation of voltage-dependent and Ca_i^{2+}-dependent fluorescence signals in three-dimensional (3-D) heart tissues via accurate measurements of light transport in the surface and internal layers of the myocardial wall. Obtaining a representative light transport model involves accurate measurements of the absorption and scattering coefficients and the anisotropy parameter, μ_a, μ_s, and g, respectively. The existence of an accurate tissue-specific light transport model is the key to signal deconvolution and the development of 3-D tomographic imaging techniques.[20,25,26,27]

There are several methods for measuring the absorption and scattering coefficients and the anisotropy parameter, μ_a, μ_s, and g, respectively. The classic method is based on measurement of diffuse reflectance R_d, the diffuse transmittance T_d, and the collimated transmittance T_c in thin tissue slices.[28] The method utilizes two integrating spheres to measure R_d and T_d and then uses a series of apertures to measure T_c. More recent methods use time-resolved measurements of local reflectance $R(\rho)$ at different distances ρ from a light source.[29,30]

One incarnation of this method described in Ref. 30 uses a sinusoidally modulated laser as the source and measures the phase some distance away at the surface of the medium with a multidistance frequency domain (MDFD) spectrometer. The local reflectance $R(\rho)$ is measured as well with a multidistance broadband spectrometer (MDBBS). While the MDFD

*Address all correspondence to: Arkady M. Pertsov, E-mail: pertsova@upstate.edu

1083-3668/2017/$25.00

method alone can be used to determine μ_a and μ_s',[29] MDFD and MDBBS together can be used to improve the accuracy of the measurements.

In this work, we set out to extract the key light scattering model parameters μ_a, μ_s, and g using an approach based on high-resolution forward-directed flux (FDF) measurements. The method is intended for isolated tissue samples and tissue phantoms, and its major advantage over the existing techniques is its extreme simplicity. The majority of measurements were carried out in pig myocardium (a close analog of the human heart), which is one of the major models used in cardiac electrophysiology to study cardiac arrhythmias using optical mapping. The measurements were carried out at 532 and 660 nm, common excitation and emission wavelengths of widely used voltage-sensitive and Ca-sensitive dyes (see discussion above).

The existing experimental information about key light scattering parameters in cardiac tissue is rather scarce and shows a high degree of scatter between different studies.[28,31,32] To date, we know of only one study in porcine heart, where all three of the key light scattering model parameters were reported[32] and which utilized the wavelengths in the neighborhood of 660 nm (see Appendix C). This makes it particularly interesting to derive these data independently using a different technique.

Although the focus of our study was on measuring light transport characteristics in porcine heart relevant for optical mapping, the new experimental approach utilized in this study may have broader applications: it can be used for the evaluation of optical parameters in turbid media as a simple alternative to collimated transmittance measurements,[32,33] reflectance-mode confocal microscopy and optical coherence tomography,[5,34–36] both requiring rather sophisticated equipment.

2 Methods

In this study, we use a thin custom-made fiber-optic probe to investigate the FDF with a 10-μm resolution. The experiments are carried out in pig myocardial wall and homogenized pig myocardial tissue, as well as in lipid-based tissue phantoms. In the vicinity of the illuminated surface, we observed a rapid decay of the light intensity with a spatial constant in the range of 100 μm, suggesting that we were likely detecting a phenomenon linked to the decay of ballistic photons. This effect was observed in the intact myocardial wall, homogenized cardiac tissue, and intralipid (IL)-based tissue phantoms.

To determine the factors affecting the rate of the fast exponent, we simulated measurements of FDF using Monte Carlo (MC) simulations. The FDF was evaluated in the physiological range of absorption and scattering coefficients, variable anisotropy parameter g, and different numerical apertures (NA) of the probe. Based on the MC model, we obtained a simple empirical formula linking the rate of the fast exponent to the scattering coefficient, the anisotropy parameter, and the NA. The predictions of the formula were tested experimentally in phantoms.

2.1 *Experimental Setup*

A schematic of the experimental setup for FDF measurements is shown in Fig. 1. The sample was illuminated from underneath with a broad collimated beam of light. The fiber-optic probe was placed over the sample and gradually advanced via a micromanipulator to measure the FDF $\psi(z)$.

The apparatus consisted of an aluminum stand (not shown) with a sample tray, the three-axis micromanipulator with attached fiber-optic probe, and the illumination system. The stand was painted flat black so as not to reflect light. The micromanipulator, bolted to the top of the stand, allowed the probe to move along x, y, and z axes as well as to rotate up to 90 deg around the horizontal axis. The fine adjustment allows the probe to be advanced into the sample in steps as small as 10 μm.

The light sources (Shanghai Dream Lasers) were a 660 nm, 600 mW laser (model SDL-LM-660-600T) and a 532 nm, 1000 mW laser (model SDL-532-1000T). To remove the nonuniformity in the 660-nm laser's beam profile, the beam was focused with a 45-mm double convex (DCX) lens ($F = 250$ mm) onto a holographic diffuser plate. The outgoing beam was collimated using an 83-mm diameter DCX lens with $F = 173$ mm (Anchor Optics AX74813) and reflected upward by a 108 mm × 145 mm × 3 mm mirror (Anchor Optics AX27536) to illuminate the tissue sample.

We used a custom-built optical probe (optrode) using the FG200LCC optical fiber (Thorlabs). The NA of the fiber and its diameter were 0.22 and 200 μm, respectively (see Appendix A for more details).

2.2 *Measuring Forward-Directed Flux*

Measuring the FDF required calibrating the position of the probe, such that the micromanipulator would read 0 when

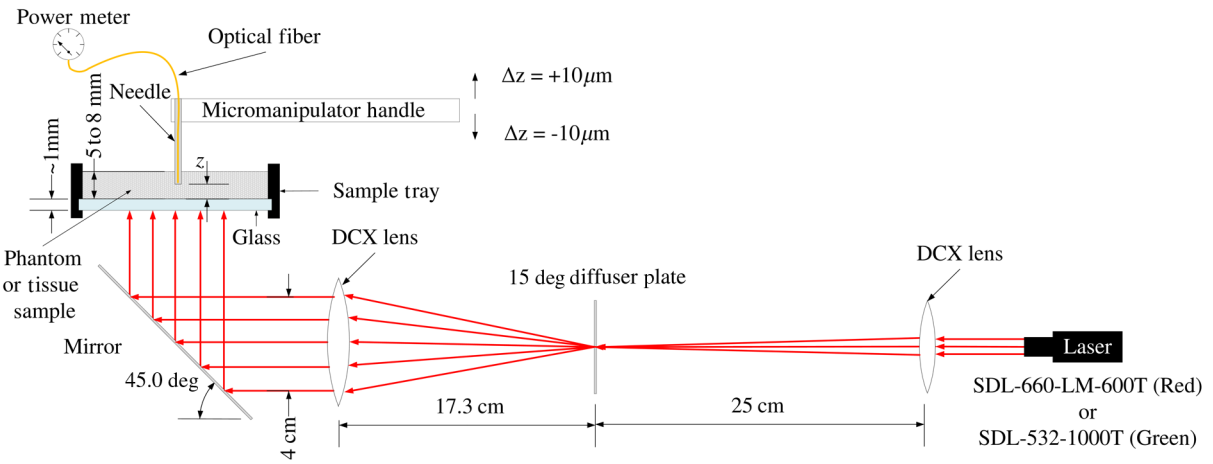

Fig. 1 Schematic of the experimental setup used for light attenuation measurments (side view).

the tip of the needle touched the glass. Next, the probe was raised and the sample (heart tissue, homogenized heart tissue, or phantom) was placed under the probe. The needle was then advanced in small steps into the sample, starting on the surface and continuing until the probe tip touched the glass bottom ($z = 0$). To keep the change in intensity more uniform over the entire thickness of the medium, the step size (Δz) varied with z, so that the change in power between steps did not exceed 10%. The initial value of Δz was chosen between 100 and 200 μm. When change in power between steps exceeded 10%, the step size was cut in half. As a result, Δz was reduced to 50, 20, and 10 μm at depths of $z = 1$ mm, 200 and 100 μm, respectively.

2.3 *Tissue Samples*

All tissue experiments were performed in accordance with National Institutes of Health Guidelines in the use of laboratory animals and approved by the SUNY Upstate Medical University Animal Care and Use Committee. Female Yorkshire pigs (26 to 32 kg) undergoing 48-hr sepsis studies were anesthetized using a continuous infusion of ketamine/xylazine. Our choice of the specimens was determined in part by the availability of freshly harvested hearts from another study, which enabled us to achieve our objectives without sacrificing additional animals. Upon completion of the study, pigs were euthanized and the hearts were removed. The right ventricle was dissected from each heart and laid flat on a piece of glass with the epicardial side facing the light source and the endocardial side facing the fiber-optic probe. A small incision was made in the endocardial side with a scalpel at the fiber-optic probe insertion site to prevent a dimple from forming on the surface as the flat tipped and comparatively large-diameter needle went in.

In some of the experiments, the measurements of FDF were carried out in homogenized tissue. The heart ventricles were separated from the valves, veins, arteries, atria, auricle, and fat. The 100 to 200 cc of isolated muscle tissues were then homogenized for 2 to 3 min into a fine paste by the Omni Macro ES digital programmable homogenizer by Omni International. The homogenized tissue was then placed in the sample tray and spread to an even thickness of 5 to 10 mm. The measurement protocol for these samples was the same as that used for the intact heart tissue.

2.4 *Phantoms*

We used a mixture of India ink, as the absorber, with IL 20% emulsion (Sigma Aldrich), as the scattering media. The experiments were conducted for IL concentration of 8% being close to the scattering properties of cardiac tissue at 660 nm, see discussion below.

2.5 *Monte Carlo Light Transport Simulations*

To simulate measurements of FDF, ψ, at different depths, $\psi(z)$, using optical fibers of varying NA (i.e., varying maximum acceptance angle, θ, where $\mathrm{NA} = n \sin(\theta)$ and $n =$ index of refraction of the tissue), we performed MC simulations using the open-source software packages Monte Carlo modeling of photon transport in multi-layered tissues (MCML)[37] and CONV.[38]

Using MCML, we obtained the tissue response to an infinitely narrow light beam. The "total transmittance" MCML routine was modified to allow simulation of the FDF at any given depth z inside the tissue. This was achieved by allowing user-defined placement of the z-plane, where total transmittance was calculated, which, in the original routine, was fixed at the tissue's rear surface. The output of the modified program produced the FDF $\psi(z, r, \alpha)$ as function of the distance, r, from the beam axis, and the angle of photon incidence α with respect to a line normal to a given z-plane (grid spacing, $\Delta\alpha = 1$ deg; $\alpha =$ 0 deg to 90 deg).

The function $\psi(z, r, \alpha)$ was then convolved using the CONV package to simulate broad-field illumination. We simulated a circular, flat incident beam of radius $R = 1.5$ cm with total incident energy of 1.0 J. The probe was located in the center of the beam ($r = 0$). Increasing R above the set value did not affect the convolution results. This suggests that the condition of uniform broad-field illumination was satisfied. To obtain responses for probes with different NAs, the function $\psi(z, r = 0, \alpha)$ was convolved with the function representing the angular sensitivity of the respective probe.

The following parameters were used as inputs to the program: (1) the photon absorption coefficient, μ_a; (2) the photon scattering coefficient, μ_s; (3) the scattering anisotropy factor, g; (4) the refractive index of both the tissue (n_{tissue}) and surrounding ambient air medium ($n_{\mathrm{air}} = 1.0$); and (5) the thickness of the tissue, d. The numerical values of the parameters were chosen based on the literature data obtained for cardiac tissues in different species for wavelengths ranging from 650 to 700 nm (see Table 5, Appendix C). The absorption coefficient was held constant at $\mu_a = 0.1$ mm^{-1} for all simulations. This value is approximately the median of the reported values (0.018 to 0.150 mm^{-1}). The values of μ_s were set at 5, 10, and 20 mm^{-1}, which cover the range of values reported in the literature (6.27 mm^{-1} in Ref. 31, 10.4 mm^{-1} in Ref. 32, and 21.8 mm^{-1} in Ref. 28). The refractive index in the tissue was set at 1.4 following Ref. 39. (Respective measurements were carried in bovine muscle illuminated with 632.8-nm light.)

We explored how the FDF, $\psi(z)$, as function of depth ($z = 0$ to 5 mm), was affected by the anisotropy coefficient, g (from 0.10 to 0.99), and fiber-optic probe maximum acceptance angle, α (from 1 deg to 36 deg). The tissue thickness, d, was set at a value of 5.0 mm. For each MCML simulation, a total of 100,000,000 photon packets were launched.

3 Results

3.1 *Measuring $\psi(z)$ in Heart Tissue*

Representative samples of forward flux measurements in the intact pig right ventricular wall at 660 and 532 nm are shown in Fig. 2(a). The normalized FDF is plotted on a log scale. The data points for 530 nm lie well below those for 660 nm, which reflects the higher rate of attenuation of green light as compared with red light. However, both curves have an important similarity. Each has a steeper slope at smaller z and a lower one at larger z suggesting that the curves represent a sum of two decaying exponents.

Confirmation that the data in Fig. 2(a) are indeed in accordance with the sum of two-exponential decay functions as presented in Eq. (1) are obtained by using the FIT function of MATLAB,

$$\psi(z) = k_1 e^{-z/\delta_1} + k_2 e^{-z/\delta_2}. \quad (1)$$

Note that for normalized data, $k_1 + k_2 = 1$. The weighting of each point was set to the inverse of its value. Such weighting

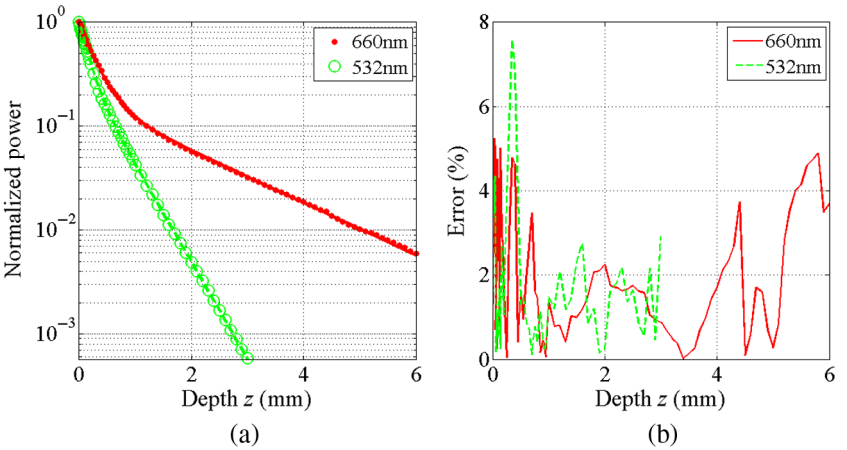

Fig. 2 (a) FDF plots at 660 nm (red) and 532 nm (green) in pig right ventricular wall. Red and green solid lines show the respective two-exponent fits. (b) Relative error of the fits.

enabled accurate fitting of the smaller valued points of the slow exponent, which otherwise would not be given the same consideration as the larger values of the fast exponent. Figure 2(b) shows the error of the two-exponent fit of the data shown in Fig. 2(a). One can see that the maximum error is below 8%, and the average error is about 1.5%, which supports the two-exponent function hypothesis.

Similar measurements were carried out in different locations, in five different hearts. The recording sites were chosen primarily across the apical section of the right ventricle, which lacks fat patches and large blood vessels. An example of the measurement sites we chose is shown in Fig. 3, which depict the endocardial and epicardial surfaces of the right ventricle

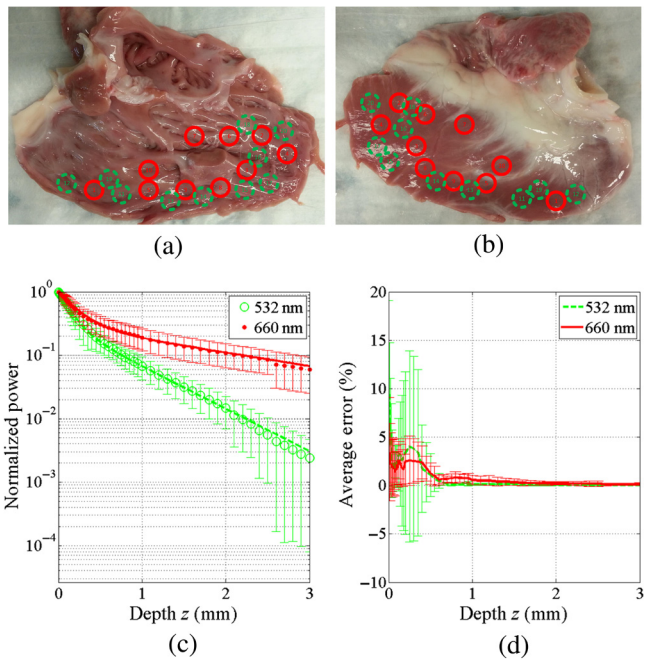

Fig. 3 Picture of (a) endocardial and (b) epicardial sides of pig right ventricular wall in one of the hearts. The red-solid circles represent measurement sites for 660-nm light, and the green-dashed circles represent measurement sites for 532-nm light. (c) Plot of average FDF data across all recording sites for 660 and 532-nm light. (d) Averaged fit error.

in one of the hearts and all the measurement sites. The number of measurements conducted on each heart was 20 (10 with red light and 10 with green light).

Figure 3 shows the averaged FDF data and fit curves in one of the preparations. It is notable that while the scatter of the light intensity at any given depth is quite significant, the accuracy of the individual fits [see Fig. 3(d)] remains relatively high. This reflects the fact that while the optical properties of the tissue vary from one location to another, $\psi(z)$ remains as a two-exponential function. The average fit parameters k_1, δ_1, and δ_2 for different hearts and their standard deviations for 532- and 660-nm light are shown in Table 1 for five hearts each with 10 measurements for red and green light, for a total of 100 measurements.

Due to signal normalization to $\psi(0)$, the parameter k_2 is calculated as $k_2 = 1 - k_1$. The attenuation length for ballistic photons δ_1 at 530 nm is almost two times smaller than at 660 nm (0.13 versus 0.24 mm). The difference is even greater for δ_2 (0.58 versus 2.1 mm). The observed differences are the manifestation of reduced light absorption and scattering at longer wavelengths.

The interpretation of the long spatial constant is rather straightforward. It represents a spatial decay of fluence rate in the diffuse regime, with δ_2 being the attenuation length commonly symbolized as δ in the literature. Indeed, our experimentally measured values of δ_2 are within the range of values reported in Refs. 28, 31, 32, and 40 for cardiac tissue (1.4 to 3.6 mm). The origin of the fast exponent is less obvious. The numerical value of δ_1 is not reported in the literature. However, according to our experiments, its inverse (δ_1^{-1}) is between 5 and 8 mm^{-1}, which is not too far off from the values that are reported in Refs. 28, 31, and 32 for the scattering coefficient in biological tissues (6.27 to 21.8 mm^{-1}). This suggests that δ_1 may represent the decay of ballistic photons in the tissue. It may also reflect a heterogeneity of the optical properties of the myocardial surface layer or both.

To assess the potential contribution of myocardial heterogeneity on $\psi(z)$, we carried out the following experiment. After measuring $\psi(z)$ in intact heart tissue, the tissue was homogenized, and the experiments were repeated. Figure 4 compares $\psi(z)$ before and after homogenization. If the first exponent was the result of optical heterogeneity, after homogenization, we would have observed a significant reduction, or the complete

Table 1 Optical characteristics of pig ventricular myocardium at 660 and 532 nm. Five hearts were examined and 10 measurements for red and green light each were taken for a total of 100 measurements.

Wavelength (nm)	k_1	δ_1 (mm)	δ_2 (mm)
660	0.76 ± 0.05	0.24 ± 0.05	2.1 ± 0.45
530	0.71 ± 0.08	0.13 ± 0.02	0.58 ± 0.13

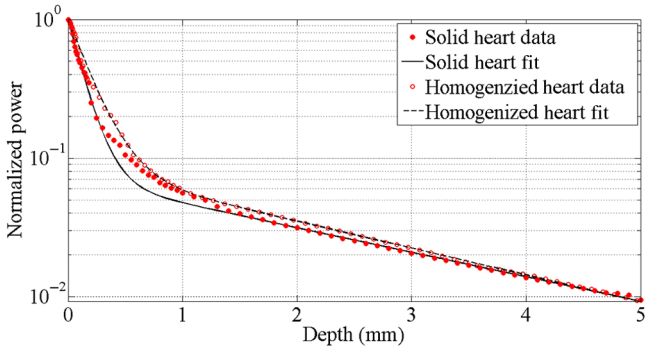

Fig. 4 Comparison of $\psi(z)$ measured in the same heart, once as intact tissue and once after being homogenized, illuminated with 660-nm light. The data were collected with the optrode made from the 25-gauge needle and the FG200LCC optical fiber (NA = 0.22).

Table 2 Optical characteristics of intact and homogenized pig ventricular myocardium at 660 nm.

Tissue	δ_1 (mm)	δ_2 (mm)
Intact	0.24 ± 0.05	2.1 ± 0.45
Homogenized	0.25 ± 0.10	2.1 ± 0.28

disappearance, of the fast exponent. However, this was not the case.

One can see that after homogenization, the first exponent is largely preserved, which suggests that it is not the result of tissue heterogeneity. The average values of δ_1 and δ_2 obtained in intact and in homogenized tissues ($N = 100$ and 5, respectively) at 660 nm are compared in Table 2. The differences are insignificant, suggesting that the process of homogenization does not affect the decay constants.

3.2 *Monte Carlo Simulations*

To determine a potential link between the fast exponent and the rate of decay of ballistic photons, we carried out MC simulations of FDF measurements reproducing our experimental protocol. The results are presented in Fig. 5.

Figure 5(a) shows simulated $\psi(z)$ for two probes with different NAs. One had an NA = 0.22, matching the probe used in our experiments, whereas the second probe had a much smaller NA (NA = 0.024) and consequently should accept fewer diffuse photons. The parameters (see figure legend) were chosen to be close to those reported in the literature for pig myocardium.[31] As in the tissue experiments, both plots could be well approximated with the sum of two exponents [see fit error plots in Fig. 5(b)].

The slope of the slow exponent δ_2 is nearly identical in both cases (for NA = 0.024 and for NA = 0.22). As expected, δ_2 corresponds to attenuation length reflecting the decay of diffuse photons

$$\delta_2 = [3\mu_a(\mu_a + \mu_s')]^{-\frac{1}{2}}, \tag{2}$$

where μ_a and μ_s' are the absorption and reduced scattering coefficients, respectively. Note that for Eq. (2) to be valid, $\mu_s' \gg \mu_a$ which is satisfied in our case.

We compared the δ_2 predicted by Eq. (2) with the respective value obtained from fitting the FDF, $\psi(z)$. The value of μ_s' was calculated using the following equation:

$$\mu_s' = \mu_s(1 - g), \tag{3}$$

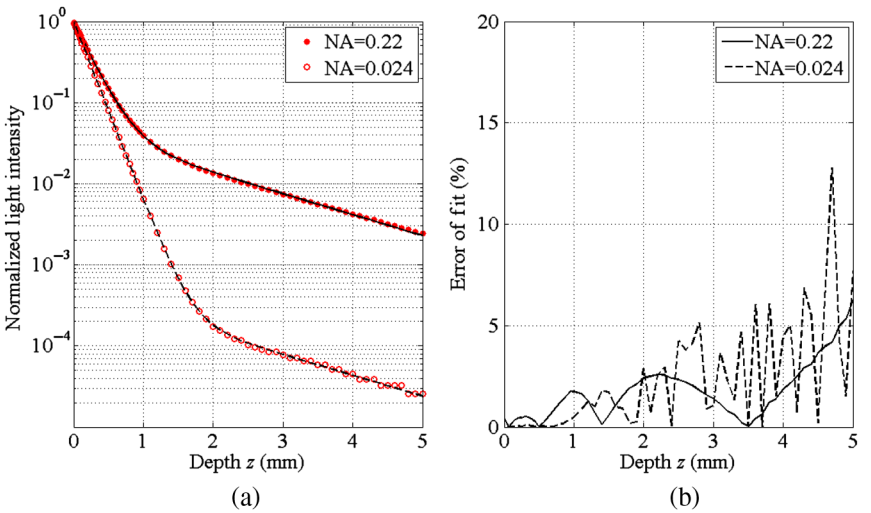

Fig. 5 (a) MC simulations of the FDF, $\psi(z)$, for fiber-optic probes with large (NA = 0.22) and small (NA = 0.024) NAs ($\lambda = 660$ nm, $\mu_s = 5$ mm^{-1}, $\mu_a = 0.1$ mm^{-1}, $g = 0.80$) and (b) the error of curve fit is shown on the right.

where μ_s and g are the scattering coefficient and anisotropy parameter, respectively. The difference between the predicted and the "experimental" values of δ_2 was within 3%.

The slopes of the fast exponents were also similar. Despite a 10-fold difference in the NA (NA = 0.22 and NA = 0.024), the values of δ_1 were 0.24 and 0.20, respectively. The only significant difference between the two cases was in the distribution of the weights between the fast and the slow exponents, which could be anticipated. Indeed, the weight of the slow exponent k_2 obtained using the probe with larger NA should be greater because it accepts a larger portion of diffuse photons.

Notably, the shorter δ_1 obtained from the fit was very close to the rate of decay of ballistic photons $\delta_b = 0.196$ mm for the given values of μ_a (0.1 mm^{-1}) and μ_s (5 mm^{-1})

$$\delta_b = (\mu_a + \mu_s)^{-1}. \tag{4}$$

This result suggests that for a given set of optical characteristics, the decay rate is not significantly influenced by diffuse photons despite relatively large NAs of the probe. This was unexpected considering that the NA for measuring δ_b is usually 10^{-3} smaller than that of NA used in our experiments.

To determine how well this observation holds at different parameters, we carried out a series of MC simulations by varying the scattering coefficient μ_s, the anisotropy coefficient g, and the NA of the probe NA.

The simulation results are shown in Fig. 6. Panel (a) shows the dependence of δ_1^{-1} on g at three different values of μ_s for a probe with NA = 0.22, which we used in our experiments. Panel (b) shows the same data after normalization by μ_s. Panel (c) shows the effect of NA on δ_1^{-1} at different g for $\mu_s = 10$ mm^{-1}.

Our findings can be summarized as follows:

1. δ_1^{-1} is proportional to μ_s for all values of g tested. Indeed, Fig. 6(b) shows that after normalization by μ_s, the data points from the three sets in panel (a) fall on top of each other for all values of g.
2. At smaller values of g, $\delta_1^{-1} \approx \mu_s$. The range of g, where this holds [the plateau region in Figs. 6(a) and 6(b)], is rather wide and becomes even wider as the NA of the probe becomes smaller [see Fig. 6(c)]. For $g < 0.7$ and a probe with NA = 0.22, the difference between δ_1^{-1} and μ_s is <10%.
3. The dependence of δ_1^{-1} on μ_s, g, and the optical probe's maximum acceptance angle, θ', (in radians) can be fitted using the following simple empirical formula:

$$\delta_1^{-1} = \mu_s \left[1 - \exp\left(\frac{g-1}{\theta' g}\right)\right]. \tag{5}$$

The accuracy of the fit can be appreciated from Fig. 6, panel (b), which shows plots of Eq. (5) for δ_1^{-1}/μ_s versus the anisotropy coefficient g, superimposed on the normalized MC simulation data. Please note that all the above is valid for $\mu_s \gg \mu_a$, the condition that is usually satisfied in the cardiac and other biological tissues.[41]

3.3 *Using Forward Directed Flux Measurements for Estimating μ_s, μ_s', and μ_a*

In cardiac tissues, the reported values of g fall in the range between 0.78[31] and 0.96.[28] In pig myocardium, at 700 nm, it is reported to be around $g = 0.91$.[32] Using this value of g as well as the experimentally derived values of δ_1 and δ_2, we estimated the key optical parameters of the tissue, such as μ_s, μ_s', and μ_a and compared them with the respective values reported in the literature. The value of μ_s was obtained from Eq. (5) by substituting the numerical value of g and the average value of δ_1 obtained in our experiments. Then, we calculated the reduced scattering coefficient μ_s' from Eq. (3) using the earlier derived value of μ_s. Finally, we plugged μ_s' into Eq. (2) and solved for μ_a. The respective results are shown in Table 3.

One can see that our estimates of all three parameters are consistent with the data reported in the literature for pig myocardium obtained using completely different techniques. The difference between our data and respective values obtained in Ref. 32 are <8% for μ_s and μ_s', and <15% for μ_a, which can be the result of myocardial heterogeneity and difference in wavelength (Data from the literature was obtained at 700 nm, and ours was obtained at 660 nm).

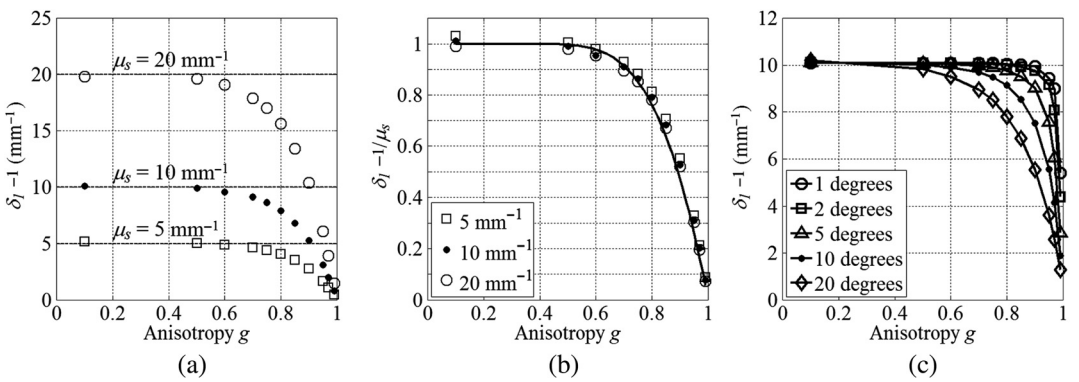

Fig. 6 Data from the MC simulations. (a) The dependence of δ_1^{-1} on anisotropy g for $\mu_s = 5$, 10, and 20 mm^{-1}. (b) The data from panel A replotted with δ_1^{-1} normalized by dividing by μ_s. (c) The dependence of δ^{-1} on anisotropy g for five different values of the optical probe maximum acceptance angle α (here, $\mu_s = 10$ mm^{-1}). In panels A and B, the NA of the probe was NA = 0.22 ($\alpha \approx 10$ deg). The absorption coefficient was $\mu_a = 0.1$ mm^{-1} for all plots.

Table 3 Optical parameters of pig myocardial tissue at 660 nm.

	μ_s (mm^{-1})	μ_s' (mm^{-1})	μ_a (mm^{-1})
Estimated from Swartling et al.[32]	9.6	0.87	0.08
	10.4	0.94	0.094

3.4 *Using Forward Directed Flux Measurements for Estimating μ_s', μ_a, g and μ_s in Intralipid-Based Tissue Phantoms*

As we will show below, the values of μ_s', μ_a, g, and μ_s can be obtained from FDF even without prior knowledge of g. All we need is to repeat the measurements of $\psi(z)$ after adding a known amount of absorber. By comparing the changes in δ_2 after adding an absorber, one can determine the values of μ_s' and the absorption coefficient μ_a. This method is known in the literature as the added absorber method.[42] Indeed, adding an absorber with a known absorption coefficient $\Delta\mu_a$ changes the attenuation length δ_2 to a new value $\delta_{2\Delta}$ that can be expressed using the following formula:

$$\delta_{2\Delta} = [3(\mu_a + \Delta\mu_a)(\mu_a + \Delta\mu_a + \mu_s')]^{\frac{1}{2}}. \quad (6)$$

Solving Eqs. (2) and (6) together yields the values of μ_a and μ_s'. Subsequently, one can solve Eqs. (3) and (5) together to derive g and μ_s. To illustrate the feasibility of this approach, we carried out experiments in IL-based tissue phantoms.

Figure 7 shows sample plots of $\psi(z)$ in 4% IL phantom with and without an absorber (India ink) at 660 nm (panel A) and 532 nm (panel C). The data fit average error was within 1% to 2% [panels (b) and (d)]. The addition of an absorber has a negligible effect on δ_1 because $\Delta\mu_a$ is very small. In contrast, the values of δ_2 undergo a significant change, which is roughly proportional to the square root of μ_a [see Eq. (6)].

Table 4 shows the values of δ_1 and δ_2 as well as estimated values of μ_s', μ_a, g and μ_s for different phantoms at 660 and 532 nm. Notably, the values of g obtained in our experiments

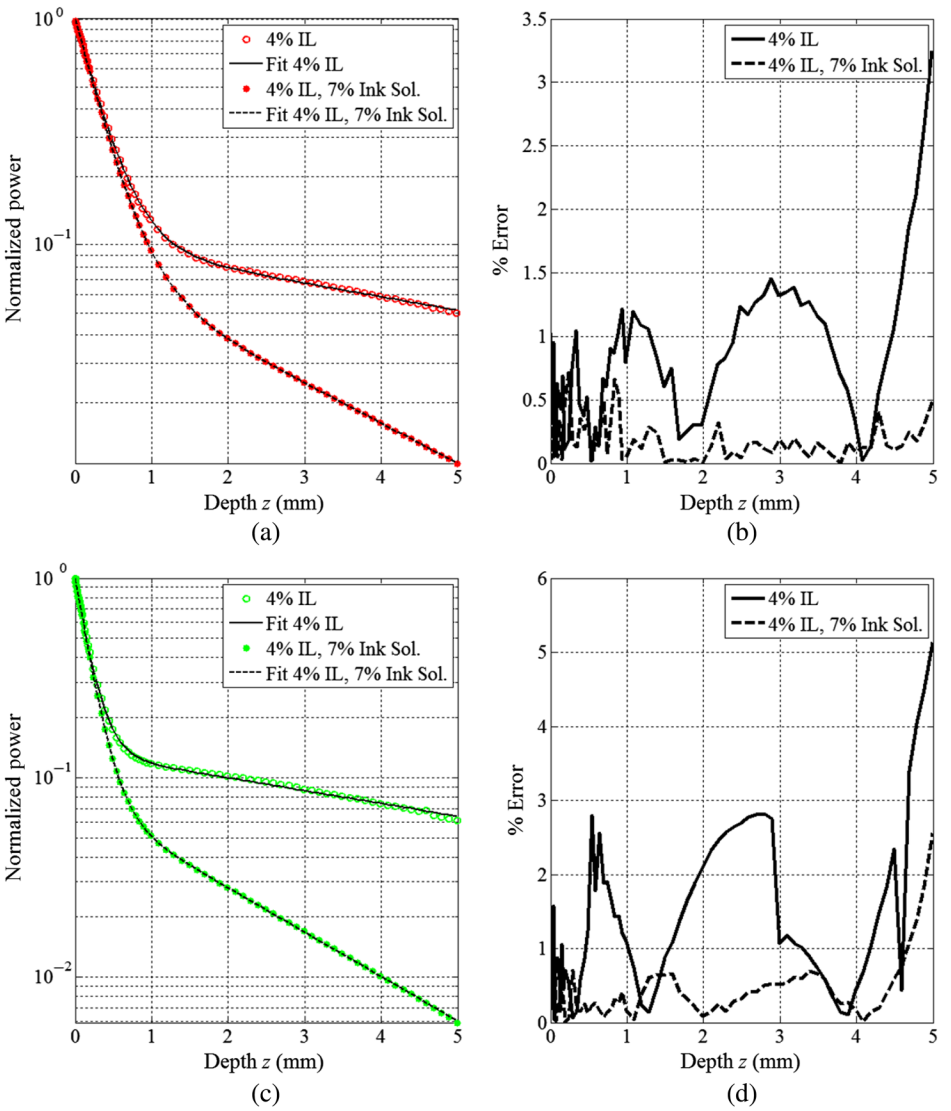

Fig. 7 Forward-directed flux measurements in phantoms at 660 and 532 nm. The data was collected with the optrode made from the 25G needle and the FG200LCC optical fiber (0.22 NA). (a) shows the FDF measurements for 660 nm with the corresponding error of the fit in panel (b), (c) shows the FDF measurements for 532nm light with the corresponding error of fit in panel (d).

Table 4 Optical characteristics of IL phantoms at 660 and 532 nm derived from the FDF measurements.

λ (nm)	Concentrations	δ_1 (mm)	δ_2 (mm)	μ_a (mm^{-1})	μ_s' (mm^{-1})	μ_s (mm^{-1})	g
660	8% IL	0.17	5.30	0.006	1.83	5.91	0.69
	8% IL, 7% ink	0.18	1.79	0.055		5.62	0.67
532	8% IL	0.10	5.85	0.003	2.99	11.5	0.74
	8% IL, 7% ink	0.10	1.33	0.066		11.5	0.74

are within 8% of the values reported in the literature (0.64 for red light and 0.73 for green light) for this particular type of IL.[43] In addition, they reproduce the increase in g due to the reduction of the illumination wavelength from 660 to 532 nm.

To compare our values of μ_s with those reported in the literature, we also estimated values of μ_s for 20% emulsion IL under the assumption that μ_s is proportional to IL concentration. Using the scattering coefficient for undiluted IL given in the literature ($\mu_s = 70$ mm^{-1} for red light and 123 mm^{-1} for green light), we can expect $\mu_s = 5.6$ mm^{-1} for red light and $\mu_s = 9.84$ mm^{-1} for green light at 8% concentration. The estimated values are close to the measured values in Table 4.

4 Discussion

In this study, we use a thin custom-made fiber-optic probe to investigate the FDF with a 10-μm resolution in pig myocardial wall. The measurements were carried out at 660 and 532 nm, which represent the most common range of the excitation and emission wavelengths of fluorescent voltage-sensitive and Ca_i^{2+}-sensitive probes used in cardiac electrophysiology.[7,44] We show that the FDF can be described as the sum of two exponents with distinctly different decay rates. In the vicinity of the illuminated surface, we observed a rapid decay of the light intensity with the decay constant δ_1 in the range of 100 to 200 μm for green and red lights, respectively. The slower exponent δ_2 had a decay constant of 5 to 10 times longer. A similar effect was observed in homogenized cardiac tissue and IL-based tissue phantoms.

A similar two-exponential decay was previously observed in collimated transmission experiments.[33] In these experiments, the fast exponent represents the decay of ballistic photons. However, this interpretation does not fully apply to our experimental data. There are the following two major differences between collimated transmittance and our experiments: (a) in our experiments, the probe is inside and not outside the specimen and (b) the NA of the optical fiber in our experiments was about two orders of magnitude larger than the NA typically used in collimated transmittance experiments. Thus, it would be reasonable to expect that in our experiments, δ_1 is affected by the gradient of diffuse photons near the surface.

It is notable that previous measurements of FDF did not report the fast exponent[7,42] and describe only the slow exponent. The decay constant of the slow exponent δ_2 is typically referred to in the literature as the "attenuation length."[7,40] The value of δ_2 measured in our cardiac tissue experiments is comparable with the attenuation lengths reported in the literature[7,28,45] at similar wavelengths. Considering that δ_1 is in the order of 100 μm, the fast exponent can be easily missed, unless the probe is advanced at very small increments near the surface. In our experiments, the increments of z near the surface were as low as 10 μm, which enabled us to reconstruct the fast exponent.

To determine the factors affecting the rate of the fast exponent, we reproduced our experiments using MC simulations. The FDF was evaluated in the physiological range of absorption and scattering coefficients, variable anisotropy parameter g, and different NAs of the probe.

One of the unexpected findings was that despite the relatively large NA of the probe and the existence of a gradient of diffuse photons near the illuminated surface, as long as g was not too large, the decay constant δ_1 still determined the rate of decay of the ballistic photons. The MC simulations show that in turbid media with $g < 0.7$, the value δ_1^{-1} yields a quite accurate (error <10%) estimate of μ_s. Thus, simple FDF measurements using a fiber-optic probe provide an alternative to the more sophisticated methods that are usually used to assess the scattering coefficient. Specifically, such an approach would be useful for estimating μ_s in lipid-based phantoms that are characterized with a relatively low anisotropy parameter.[43]

It is interesting that the dependence of the rate of the fast exponent on the scattering coefficient, the anisotropy parameter g, and the NA of the probe can be linked by a simple empirical formula without any adjustable parameters. The formula predicts MC simulation results in a broad range of parameters. It works particularly well at NA ≤ 0.22. We started observing deviations only at NA > 0.34. We tested the predictions of the formula in the cardiac tissue and in well-characterized, IL-based tissue phantoms. The tests results were in agreement with the data reported in the literature.

Our findings pave the way to an alternative method for determining major optical parameters in turbid media based exclusively on FDF measurements. The new approach allows the utilization of the same simple experimental setup for measuring all key optical parameters including anisotropy g. Previously, however, measurements of μ_s and g required completely different experimental setups than those used for measurements of μ_a and μ_s'. The simplicity of the experimental approach described here as well as the ability to utilize the same setup for all measurements can make it a viable alternative to existing methods. Although the feasibility of the new approach was experimentally verified only in IL-based tissue phantoms with known values of μ_a, μ_s, and g, it would be reasonable to assume that it would work in homogenized tissues as well. Indeed, our data suggest that the values of δ_1 and δ_2 in the homogenized tissues are not significantly different from the respective values in the intact tissue (see Table 2).

The results of our work shed a new light on light transport in the vicinity of the myocardial surface. This can be particularly useful for the interpretation of the optical recordings of cardiac excitation obtained using voltage-sensitive dyes, known as optical mapping, as well as for the development of 3-D tomographic approaches.[8] One of the potential applications of our findings is

obtaining an accurate description of voltage distribution in the vicinity of the myocardial surface during strong defibrillation shocks. According to theoretical models, the transmembrane voltage should fall off rapidly with depth,[45] which makes the detailed knowledge of light transport near the illuminated surface critically important for an accurate description of this phenomenon. Our study adds a potentially useful tool to the arsenal of existing methods, which could help to fill this gap.

Appendix A: Manufacturing and Characterization of the Optical Probes

The optical fibers were threaded through a needle mounted on a 1-ml syringe and secured with super glue. A 25-gauge needle was used for the 200-μm fibers. To pass the fiber through the shaft of the needle, the jacket and coating were removed. We then applied Norland Optical Adhesive 81 (NOA81) from Thorlabs, which protected the fiber from chipping and secured it within the needle. The fiber and needle were both cleaned prior to application of the adhesive; then, a small amount of NOA81 was poured into the needle and cured with a UV light source. Care was taken to ensure that the tip of the probe was covered with a protective layer of adhesive. The tip was then sanded flat using 5, 0.3, and then 0.05 μm lapping film (Digi-Key). The probe was continuously inspected under a microscope to ensure flatness and that the layer of NOA81 had been sufficiently polished to remove any imperfections. The fiber was attached to an optical sensor S120C (or an S150C for measurements at lower intensity) connected to a PM100D optical power meter, all from Thorlabs.

The angular sensitivity of the probes was measured by rotating the optrode with respect to the light beam as shown in Fig. 8(a). To approximate the change in refractive index at the probe/tissue interface, the tip of the probe was immersed in a petri dish containing normal saline (0.9% w/v NaCl). Figure 8(b) shows the relative light intensity as a function of angle, for all probes measured at 532 and 660 nm.

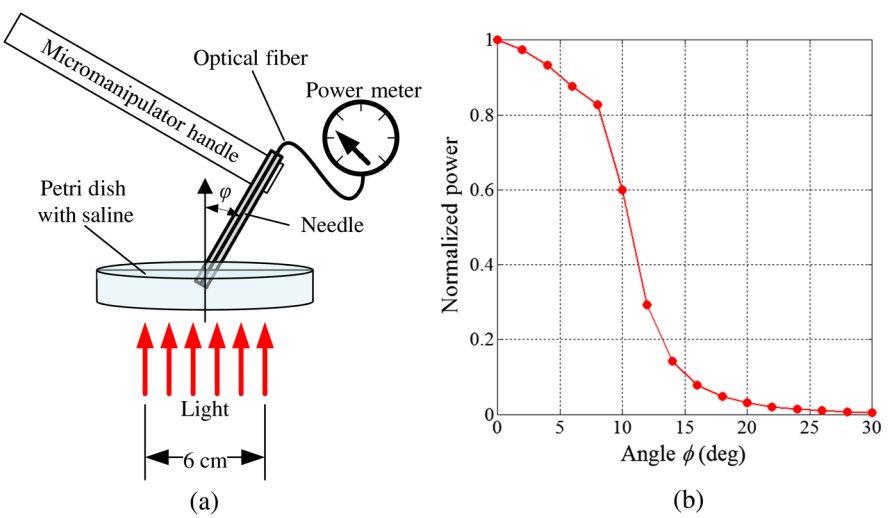

Fig. 8 Measurement of the angular sensitivity of the probe. (a) Schematic of the experimental setup and (b) angular sensitivity of the 25-gauge needle optical probes at 660 nm.

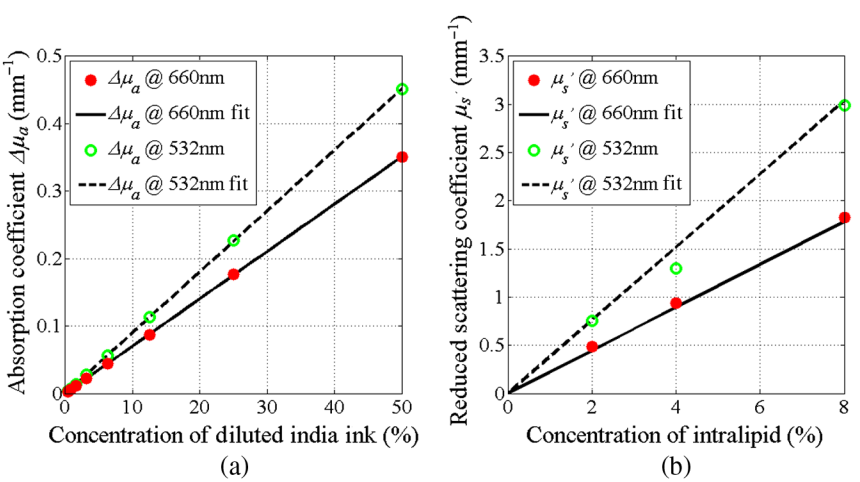

Fig. 9 Effect of ink concentration on absorption coefficient (a) and IL concentration on reduced scattering coefficient (b) for 660- and 532-nm light.

As expected, optrodes utilizing fibers with higher NA had significantly wider acceptance angles.

Appendix B: Characterization of Phantoms

The μ_a of the solution of India ink in water was characterized using a DU730 Beckman Coulter spectrophotometer, and the μ_s' of the IL was characterized using the added absorber method.[42] Figure 9 shows the absorption coefficient $\Delta\mu_a$ of the solution as a function of ink concentration for 660- and 532-nm light. The equation of the fit line is

$$\Delta\mu_a = 0.007\, C_{ink}, \tag{7}$$

for 660-nm light and

$$\Delta\mu_a = 0.009\, C_{ink}, \tag{8}$$

for 532-nm light, where C_{ink} is the concentration in water (in percent). For our experiments, we chose a concentration of 7% that yields $\Delta\mu_a = 0.049$ mm^{-1} for red and 0.063 mm^{-1} for green light, respectively, which is roughly the median of the values of μ_a for heart tissue reported in Refs. 28, 31, 32, 40, and 46.

Appendix C: Optical Parameters of Heart Tissue

The values of μ_a, μ_s, g, and μ_s' for heart tissue at 660 to 700 nm reported in the literature and obtained using different experimental techniques are shown in Table 5.

Disclosures

The authors have no relevant financial interests in the paper and no other potential conflicts of interest to disclose.

Table 5 Optical parameters of heart tissue as reported in the literature.

Source	Wavelength (nm)	μ_a (mm^{-1})	μ_s (mm^{-1})	g	μ_s' (mm^{-1})	Species
Swartling et al.[32]	660	0.146	—	—	0.920	Pig
	700	0.094	10.4	0.91	0.878	
Walton et al.[40]	650 to 700	0.032	—	—	0.899	Pig
Ding et al.[28]	669	0.150	27.1	0.95	1.355	Rabbit w/Rh237 and Oregon Green
		0.100	21.8	0.96	0.872	Rabbit w/Di-4-ANEPPS
Srinivasan and Singh[31]	670	0.018	6.27	0.78	1.38	Sheep

Acknowledgments

We would like to thank Dr. Steven Jacques at OHSU in Portland, Oregon, for his helpful advice. We would also like to thank Gary Nieman, Kathy Snyder, Josh Satalin, and Sumeet Jain at SUNY-UMU for providing us with pig hearts, and Robert Pulz at the Binghamton University (New York) student machine shop for using his extensive knowledge of machining and fabrication techniques to help us take our ideas from theory to reality. The study was supported by the Hendricks bridge grant to AMP.

References

1. D. Rosenbaum and J. Jalife, *Optical Mapping of Cardiac Excitation and Arrhythmias*, Wiley, New York (2001).
2. M. Canepari, D. Zecevic, and O. Bernus, *Membrane Potential Imaging in the Nervous System and Heart*, 2nd ed., Vol. **859**, Springer, New York (2015).
3. S. Dhein, F. Mohr, and M. Delmar, *Practical Methods in Cardiovascular Research*, Springer Link, New York (2005).
4. W. T. Baxter et al., "Visualizing excitation waves inside cardiac muscle using transillumination," *Biophys. J.* **80**(1), 516–530 (2001).
5. D. Gareau et al., "Noninvasive imaging of melanoma with reflectance mode confocal scanning laser microscopy in a murine model," *J. Invest. Dermatol.* **127**(9), 2184–2190 (2007).
6. K. Wang et al., "Cardiac tissue slices: preparation, handling, and successful optical mapping," *Am. J. Physiol. Heart Circ. Physiol.* **308**(9), H1112–H1125 (2015).
7. B. Mitrea, M. Wellner, and A. Pertsov, "Monitoring intramyocardial reentry using alternating transillumination," in *Annual Int. Conf. of the IEEE Engineering in Medicine and Biology Society (EMBC 2009)* (2009).
8. E. M. C. Hillman et al., "Depth-resolved optical imaging of transmural electrical propagation in perfused heart," *Opt. Express* **15**(26), 17827–17841 (2007).
9. M. Radisic et al., "Optical mapping of impulse propagation in engineered cardiac tissue," *Tissue Eng. Part A* **15**(4), 851–860 (2009).
10. M. G. Klein, A. Lacampagne, and M. F. Schneider, "Voltage dependence of the pattern and frequency of discrete Ca^{2+} release events after brief repriming in frog skeletal muscle," *Proc. Natl. Acad. Sci. U. S. A.* **94**(20), 11061–11066 (1997).
11. R. Arora et al., "Arrhythmogenic substrate of the pulmonary veins assessed by high-resolution optical mapping," *Circulation* **107**(13), 1816–1821 (2003).
12. W. Boesmans, M. M. Hao, and P. V. Berghe, "Optical tools to investigate cellular activity in the intestinal wall," *J. Neurogastroenterol. Motil.* **21**(3), 337–351 (2015).
13. Y. Ma et al., "Wide-field optical mapping of neural activity and brain haemodynamics: considerations and novel approaches," *Philos. Trans. R. Soc. B* **371**(1705), 20150360 (2016).
14. T. Berger et al., "Combined voltage and calcium epifluorescence imaging in vitro and in vivo reveals subthreshold and suprathreshold dynamics of mouse barrel cortex," *J. Neurophysiol.* **97**(5), 3751–3762 (2007).
15. R. D. Walton et al., "Dual excitation wavelength epifluorescence imaging of transmural electrophysiological properties in intact hearts," *Heart Rhythm* **7**(12), 1843–1849 (2010).
16. C. J. Hyatt et al., "Synthesis of voltage-sensitive fluorescence signals from three-dimensional myocardial activation patterns," *Biophys. J.* **85**(4), 2673–2683 (2003).
17. B. G. Mitrea, B. J. Caldwell, and A. M. Pertsov, "Imaging excitation inside the myocardial wall," *Biomed. Opt. Express* **2**(3), 620–633 (2011).
18. A. Matiukas et al., "Near-infrared voltage-sensitive fluorescent dyes optimized for optical mapping in blood-perfused myocardium," *Heart Rhythm* **4**(11), 1441–1451 (2007).
19. A. Matiukas et al., "New near-infrared optical probes of cardiac electrical activity," *AJP: Heart Circ. Physiol.* **290**(6), H2633–H2643 (2006).
20. T. A. Csepe et al., "Human sinoatrial node structure: 3D microanatomy of sinoatrial conduction pathways," *Prog. Biophys. Mol. Biol.* **120**(1–3), 164–178 (2016).

21. W. Bian and L. Tung, "Structure-related initiation of reentry by rapid pacing in monolayers of cardiac cells," *Circ. Res.* **98**(4), e29–e38 (2006).
22. J. A. Scull et al., "Single-detector simultaneous optical mapping of V_m and $[[Ca^{2+}]_i$ in cardiac monolayers," *Ann. Biomed. Eng.* **40**(5), 1006–1017 (2012).
23. M. Shrivastav et al., "The design and use of an optical mapping system for the intracardiac electrical signaling," *Indian Pacing Electrophysiol. J.* **12**(4), 138–151 (2012).
24. I. Efimov and T. Mazgalev, "High-resolution, three-dimensional fluorescent imaging reveals multilayer conduction pattern in the atrioventricular node," *Circulation* **98**(1), 54–57 (1998).
25. A. M. Pertsov et al., "What can we learn from the optically recorded epicardial action potential?" *Biophys. J.* **91**(10), 3959–3960 (2006).
26. C. J. Hyatt et al., "Optical action potential upstroke morphology reveals near-surface transmural propagation direction," *Circ. Res.* **97**(3), 277–284 (2005).
27. V. Tuchin, *Tissue Optics: Light Scattering Methods and Instruments for Medical Diagnostics*, 3rd ed., SPIE Press, Bellingham, Washington (2015).
28. L. Ding, S. Splinter, and S. Knisley, "Quantifying spatial localization of optical mapping using Monte Carlo simulations," *IEEE Trans. Biomed. Eng.* **48**(10), 1098–1107 (2001).
29. D. Hueber et al., "Non-invasive and quantitative near-infrared haemoglobin spectrometry in the piglet brain during hypoxic stress, using a frequency-domain multi-distance instrument," *Phys. Med. Biol.* **46**(1), 41–62 (2001).
30. I. Tachtsidis et al., "A hybrid multi-distance phase and broadband spatially resolved spectrometer and algorithm for resolving absolute concentrations of chromophores in the near-infrared light spectrum," *Adv. Exp. Med. Biol.* **662**, 169–175 (2009).
31. R. Srinivasan and M. Singh, "Development of biological tissue-equivalent phantoms for optical imaging," *Indian J. Exp. Biol.* **40**(5), 531–535 (2002).
32. J. Swartling et al., "Changes in tissue optical properties due to radio-frequency ablation of myocardium," *Med. Biol. Eng. Comput.* **41**(4), 403–409 (2003).
33. A. Yaroshevsky et al., "The transition from the ballistic to the diffusive regime in a turbid medium," *Opt. Lett.* **36**(8), 1395 (2011).
34. S. Jacques et al., "Measuring tissue optical properties in vivo using reflectance-mode confocal microscopy and OCT," *Proc. SPIE* **6864**, 68640B (2008).
35. T. Collier et al., "Determination of epithelial tissue scattering using confocal microscopy," *IEEE J. Sel. Top. Quantum Electron.* **9**(2), 307–313 (2003).
36. T. Collier et al., "Sources of scattering in cervical tissue: determination of the scattering coefficient by confocal microscopy," *Appl. Opt.* **44**(11), 2072–2081 (2005).
37. L. Wang, S. Jacques, and L. Zheng, "MCML–Monte Carlo modeling of light transport in multilayered tissues," *Comput. Meth. Programs Biomed.* **47**(2), 131–146 (1995).
38. L. Wang, S. L. Jacques, and L. Zheng, "CONV—convolution for responses to a finite diameter photon beam incident on multi-layered tissues," *Comput. Meth. Programs Biomed.* **54**(3), 141–150 (1997).
39. F. P. Bolin et al., "Refractive index of some mammalian tissues using a fiber optic cladding method," *Appl. Opt.* **28**(12), 2297–2303 (1989).
40. R. Walton et al., "Experimental validation of alternating transillumination for imaging intramural wave propagation," in *Annual Int. Conf. of the IEEE Engineering in Medicine and Biology Society (EMBC 2011)*, Vol. 2011, pp. 1676–1679 (2011).
41. S. L. Jacques, "Optical properties of biological tissues: a review," *Phys. Med. Biol.* **58**(11), R37–R61 (2013).
42. B. Wilson, M. Patterson, and D. Burns, "Effect of photosensitizer concentration in tissue on the penetration depth of photoactivating light," *Laser Med. Sci.* **1**(4), 235–244 (1986).
43. R. Michels, F. Foschum, and A. Kienle, "Optical properties of fat emulsions," *Opt. Express* **16**(8), 5907–5925 (2008).
44. V. Fast and R. Ideker, "Simultaneous optical mapping of transmembrane potential and intracellular calcium in myocyte cultures," *J. Cardiovasc. Electrophysiol.* **11**(5), 547–556 (2000).
45. M. Bishop et al., "The role of photon scattering in optical signal distortion during arrhythmia and defibrillation," *Biophys. J.* **93**(10), 3714–3726 (2007).
46. R. Splinter et al., "Optical properties of normal, diseased, and laser photocoagulated myocardium at the Nd:YAG wavelength," *Lasers Surg. Med.* **11**(2), 117–124 (1991).

Anthony J. Costantino is currently pursuing a PhD in electrical engineering at Binghamton University. His research is in the area of medical instrumentation.

Christopher J. Hyatt is a physics instructor at Springfield College, Springfield, Massachusetts. His research interests are in optical mapping of the heart and in structural and functional MRI imaging in neuroscience.

Michaela C. Kollisch-Singule is a general surgery research resident at SUNY Upstate Medical University in Syracuse, New York. She obtained her MD degree in 2011 after first studying mathematics and is scheduled to complete her surgical residency in 2018. Her research focus is on the impact of sepsis on multiple organ dysfunction and the development of protective mechanical ventilation strategies.

Jacques Beaumont is a member of the research staff in the Departments of Pharmacology and Radiology of the SUNY Upstate Medical University. Also, he is an owner of Complex Biosystems Inc. His main interests are in the modeling and simulation of biological systems with a main emphasis on the heart. His work has contributed to our understanding of rotors dynamics in the heart, interpretation of bioelectric data collected in isolated cells, and the reconstruction of geometric models of physiologic structures from medical images.

Bradley J. Roth is a professor of physics at Oakland University in Rochester, Michigan. He is a fellow of the American Physical Society and is coauthor of the textbook intermediate physics for medicine and biology. His accomplishments include making the first measurements of the magnetic field of an isolated nerve axon, calculating the electric field induced in the brain during transcranial magnetic stimulation, and applying the bidomain model to study defibrillation of the heart.

Arkady M. Pertsov is a professor of pharmacology at SUNY Upstate Medical University, Syracuse, New York. His primary areas of research are the biophysical mechanisms of cardiac arrhythmias and the imaging of electrical activity in the heart using voltage-sensitive fluorescent dyes. His accomplishments include the discovery of spiral waves in the heart and the development of tomographic methods for their visualization.